Self-pumped phase conjugation in photorefractive crystals: Reflectivity and spatial fidelity

Ping Xie,[1] Jian-Hua Dai,[1] Peng-Ye Wang,[1,2] and Hong-Jun Zhang[1,2]
[1]*Laboratory of Optical Physics, Institute of Physics & Center for Condensed Matter Physics, Chinese Academy of Sciences, Beijing 100080, China*
[2]*CCAST (World Laboratory), Post Office Box 8730, Beijing 100080, China*
(Received 12 August 1996; revised manuscript received 5 December 1996)

A two-dimensional model for the self-pumped phase conjugation in photorefractive crystals is presented. Numerical simulations of the beam path for beam fanning and the self-pumped phase conjugation within the crystals show good agreement with the experimental observations. We numerically study the dependence of the self-pumped phase conjugation reflectivity and spatial fidelity on the incident angle, the position of the incident beam upon the input face, and the input wavelength, which are in good agreement with the published and our experimental results. [S1050-2947(97)09103-8]

PACS number(s): 42.65.Hw

I. INTRODUCTION

Photorefractive crystal has become an important nonlinear-optical medium. It has promising applications in image amplification [1], externally pumped and self-pumped phase conjugation (SPPC) [2], etc. Because a self-pumped phase conjugator needs no external mirror, and consists simply of a poled single photorefractive crystal, it has attracted considerable attention since the observation by Feinberg in 1982 [3]. From the experimental point of view, self-pumped phase conjugation in a single crystal can be generally classified into two geometrical configurations. One is that there exists internal reflections of the light at a corner of the crystal, e.g., the experiments in Refs. [3] and [4], and the other is that there exists no internal reflections at any corner, e.g., the experiment in Refs. [5] and [6]. Recently, experiments in cerium-doped $BaTiO_3$ demonstrated high reflectivity and high-spatial-fidelity self-pumped phase conjugation, which clearly belongs to the latter configuration [7]. A plane-wave model for the former configuration is that the phase-conjugate beam is generated in two interaction regions by means of a four-wave-mixing process, with self-generated pump beams reflecting at a corner of the crystal [8], Zozulya, Saffman, and Anderson presented a two-dimensional model which is based on the solution of nonlinear material equations and parabolic equations for optical fields with a boundary condition taken as internal reflections at a corner of the crystal [9]. A simple model for the latter configuration is stimulated backscattering two-wave mixing [10]. In Ref. [11] we present a two-dimensional model for the latter configuration, which well explains the curved beam path inside the crystal, and the high-reflectivity and high-spatial-fidelity phase conjugation observed in $BaTiO_3$:Ce.

In this paper we give a detailed description of our theory for the self-pumped phase conjugation in photorefractive crystals, and pay attention to the numerical studies of its phase-conjugate reflectivity and spatial fidelity. Up to now, on the experimental side, efforts have concentrated mostly on the quantitative measurements of the reflectivity; on the theoretical side, because of the use of plane-wave analysis, it is limited to the studies of the phase-conjugate reflectivity. Therefore, it is necessary to give a detailed theoretical analysis of the spatial fidelity of the self-pumped phase conjugation, as well as the reflectivity. In Sec. II, the theoretical model and the steady-state coupled-wave equations for the amplitudes of the plane-wave components of the input forward propagation beam and the scattered backward propagation beam are described. In Sec. III A, we show properties of the beam fanning. Sections III B and III C focus on discussions of properties of the self-pumped phase conjugation, and its reflectivity and spatial fidelity vs various externally controlled parameters, such as the incident angle, the position of the incident beam upon the crystal entrance face, and the wavelength of the beam, which show good agreement with the published [7] experimental results and our own. Section IV presents some additional experiments to verify our numerical results. Finally, in Sec. V we give conclusions.

II. THEORETICAL MODEL AND COUPLED-WAVE EQUATIONS FOR THE SELF-PUMPED PHASE CONJUGATION

Consider two coherent extraordinary polarized beams progating in a photorefractive crystal. As shown in Fig. 1, we call the beam with its main propagation direction making an acute angle with the $+z$ direction the forward beam (denoted by F), and the beam with its main propagation direction making an acute angle with the $-z$ direction the backward beam (denoted by B). The main propagation direction of the incident forward beam F forms an angle of α with the $+z$

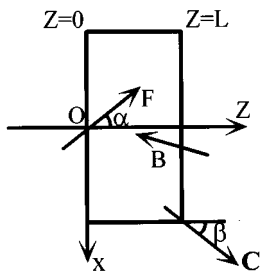

FIG. 1. Geometric configuration of two coherent extraordinary beams counterpropagating in a photorefractive crystal of thickness L.

direction, and the angle between the $+z$ axis and the crystal c axis is β. For simplicity, here we confine our analysis to two dimensions (transverse x and longitudinal z).

The electric field of the two beams is

$$E(x,z,t)=[A_F(x,z)e^{-i\omega t}+A_B(x,z)e^{-i\omega t}]+\text{c. c.}, \quad (1)$$

where ω is the optical frequency of the two beams. The complex field amplitude $A_j(x,\ z)$ ($j=F$ and B) can be decomposed into its Fourier plane-wave components, i.e.,

$$A_j(x,z)=\sum_{q_x} f_j(q_x,z)\ \exp[\pm i(q_x x+\beta_q z)], \quad (2)$$

where $+$ stands for the forward beam F and $-$ for the backward beam B and $f_j(q_x,\ z)$ is the spatial frequency distribution (or the plane-wave component) of the amplitude $A_j(x,\ z)$, with the projections of its wave vector in the x and z directions being q_x and β_q, respectively. In the above analysis we have implicitly used the paraxial approximation that the angles between the main propagation directions of the two beams and the z axis are small. The wave-vector projection q_x can be considered as a function of θ, which is defined as an angle between the wave vector and the z axis, so that the plane-wave component $f_j(q_x,z)$ can be rewritten as $f_j(\theta,\ z)$. The total electric-field amplitude of the two beams is then written as

$$A(x,z)=\sum_{\theta}\ \{f_F(\theta,z)\exp[ik\ \sin\theta x+ik\ \cos\theta z] + f_B(\theta,z)\exp[-ik\ \sin\theta x-ik\ \cos\theta z]\}+\text{c.c.}, \quad (3)$$

where $k=\omega n/c$ is the wave number of the two beams, and n is the refractive index of the crystal.

As in Refs. [12] and [13], the intensity-induced refractive index change Δn inside the crystal is modeled as a superposition of the photorefractive gratings formed by the interference of each pair of the Fourier components of the forward and the backward beams. It takes the form

$$\begin{aligned}\Delta n=&\sum_{\theta}\sum_{\theta'\neq\theta}\left\{\frac{f_F(\theta,z)f_F^*(\theta',z)+f_B^*(\theta,z)f_B(\theta',z)}{I_0(z)}\right.\\&\times\exp[ik(\sin\theta-\sin\theta')x\\&\left.+ik(\cos\theta-\cos\theta')z]\delta n_T(\theta,\theta')\right\}\\&+\sum_{\theta}\sum_{\theta'\neq\theta}\left\{\frac{f_F(\theta,z)f_B^*(\theta',z)+f_B^*(\theta,z)f_F(\theta',z)}{I_0(z)}\right.\\&\times\exp[ik(\sin\theta+\sin\theta')x+ik(\cos\theta+\cos\theta')z]\\&\left.\times\frac{\delta n_R(\theta,\theta')}{2}\right\}+\sum_{\theta}\left\{\frac{f_F(\theta,z)f_B^*(\theta,z)}{I_0(z)}\exp[2ik\ \sin\theta x\right.\\&\left.+2ik\ \cos\theta z]\frac{\delta n_R(\theta,\theta)}{2}\right\}+\text{c.c.},\end{aligned} \quad (4)$$

where $I_0(z)=\Sigma_\theta[|f_F(\theta,z)|^2+|f_B(\theta,z)|^2]$ and c.c. represents the conjugation of the second and third terms. $\delta n_T(\theta,\theta')$ [noting $\delta n_T(\theta,\theta')=\delta n_T^*(\theta',\theta)$] is a complex factor for transmission index gratings, which represents the coupling coefficient between the plane-wave components $f_F(\theta,z)$ and $f_F(\theta',z)$, or between $f_B(\theta,z)$ and $f_B(\theta',z)$; $\delta n_R(\theta,\theta')$ [noting $\delta n_R(\theta,\theta')=\delta n_R(\theta',\theta)$] is that for reflection index gratings, which represents the coupling coefficient between the plane-wave components $f_F(\theta,z)$ and $f_B(\theta',z)$, or between $f_B(\theta,z)$ and $f_F(\theta',z)$.

Note that Eq. (4) is an approximate one which does not include the effect of the dark irradiance. It is valid except at the beam edge. For a beam with a Gaussian profile, the more rigorous refractive index change Δn and its comparison with the result of Eq. (4) are given in Ref. [14].

The complex factors $\delta n_T(\theta,\theta')$ and $\delta n_R(\theta,\theta')$ are defined as

$$\delta n_T(\theta,\theta')=\frac{n_o^3}{2}r_{\text{eff}T}(\theta,\theta')E_{\text{sc}T}(\theta,\theta')\ \cos(\theta-\theta'), \quad (5a)$$

$$\delta n_R(\theta,\theta')=\frac{n_o^3}{2}r_{\text{eff}R}(\theta,\theta')E_{\text{sc}R}(\theta,\theta')\ \cos(\theta-\theta'), \quad (5b)$$

where n_o is the ordinary refractive index. $r_{\text{eff}j}(\theta,\theta')$ ($j=T,R$) is the effective electrooptic coefficient [1].

$$\begin{aligned}r_{\text{eff}j}(\theta,\theta')=&[n_o^4 r_{13}(\cos2\Theta_j-\cos2B_j)+4n_e^2n_o^2r_{42}\ \sin^2B_j\\&+n_e^4r_{33}(\cos2\Theta_j+\cos2B_j)]\ \cos B_j/2n_o^3n_e,\end{aligned} \quad (6)$$

where n_e is the extraordinary refractive index, r_{mn} ($m,n=1,2,3$) are the nonzero components of the electrooptic tensor $\Theta_T=(\theta'-\theta)/2$ is the half-angle between the wave vectors of the plane-wave components $f_F(\theta,z)$ and $f_F(\theta',z)$, and $\Theta_R=\pi/2-(\theta'-\theta)/2$ is that between wave vectors of $f_F(\theta,z)$ and $f_B(\theta',z)$. $B_T=\pi/2-[\beta-(\theta'+\theta)/2]$ is the angle between the crystal c axis and the grating wave vector $\mathbf{K}_T$ formed between the components $f_F(\theta,z)$ and $f_F(\theta',z)$, and $B_R=\beta-(\theta+\theta')/2$ is that between the c axis and the grating wave vector $\mathbf{K}_R$ formed between components $f_F(\theta,z)$ and $f_B(\theta,z)$. In the absence of any applied or intrinsic electric field, the space-charge field $E_{\text{sc}j}(\theta,\theta')$ ($j=T,R$) is given as [15]

$$E_{\text{sc}j}=-i\frac{E_{qj}E_{dj}}{E_{qj}+E_{dj}}, \quad (7)$$

where E_{dj} and E_{qj} are electric fields characteristic of diffusion and maximum space charge, respectively. $E_{dj}=k_BTK_j/q$ and $E_{qj}=eN/\varepsilon_j\varepsilon_0K_j$, where k_B is Boltzmann's constant, T the temperature, q the charge of mobile charge carriers, N the density of mobile charge carriers, and ε_0 is permittivity of free space. ε_j is the effective relative dielectric constant in the direction of the grating wave vector $\mathbf{K}_j$, which reads

$$\varepsilon_j=\varepsilon_a\ \sin^2\ B_j+\varepsilon_c\ \cos^2\ B_j, \quad (8)$$

where ε_a and ε_c are the respective relative dielectric constants perpendicular and parallel to the crystal c axis.

By using Eqs. (3) and (4) in the wave equation

$$\left(\frac{d^2}{dx^2}+\frac{d^2}{dz^2}\right)A+\frac{\omega^2}{c^2}(n+\Delta n)^2A=0, \tag{9}$$

we can derive the following coupled-wave equations in the standard slowly varying field approximation, taking into consideration only phase-matched terms, with α_L the linear absorption coefficient:

$$\begin{aligned}\cos\theta\frac{df_F(\theta,z)}{dz}=&\sum_{\theta'\neq\theta}\left\{\frac{\gamma_T(\theta,\theta')}{I_0(z)}[f_F(\theta,z)f_F^*(\theta',z)\right.\\&+f_B^*(\theta,z)f_B(\theta',z)]f_F(\theta',z)\\&+\frac{\gamma_R(\theta,\theta')}{I_0(z)}[f_F(\theta,z)f_B^*(\theta',z)\\&\left.+f_B^*(\theta,z)f_F(\theta',z)]f_B(\theta',z)\right\}\\&+\frac{\gamma_R(\theta,\theta)}{I_0(z)}[f_F(\theta,z)f_B^*(\theta,z)]f_B(\theta,z)\\&-\cos\theta\frac{\alpha_L}{2}f_F(\theta,z),\end{aligned} \tag{10a}$$

$$\begin{aligned}\cos\theta\frac{df_B^*(\theta,z)}{dz}=&\sum_{\theta'\neq\theta}\left\{\frac{\gamma_T(\theta,\theta')}{I_0(z)}[f_F(\theta,z)f_F^*(\theta',z)\right.\\&+f_B^*(\theta,z)f_B(\theta',z)]f_B^*(\theta',z)\\&+\frac{\gamma_R(\theta,\theta')}{I_0(z)}[f_F(\theta,z)f_B^*(\theta',z)\\&\left.+f_B^*(\theta,z)f_F(\theta',z)]f_F^*(\theta',z)\right\}\\&+\frac{\gamma_R(\theta,\theta)}{I_0(z)}[f_B^*(\theta,z)f_F(\theta,z)]f_F^*(\theta,z)\\&+\cos\theta\frac{\alpha_L}{2}f_B^*(\theta,z),\end{aligned} \tag{10b}$$

where $\gamma_j(\theta,\theta')$ $(j=T,R)$ is the coupling coefficient, which is defined as

$$\gamma_j(\theta,\theta')=\frac{i\omega}{2c}\delta n_j(\theta,\theta'). \tag{11}$$

Note that $\gamma_T(\theta,\theta')=-\gamma_T^*(\theta',\theta)$ and $\gamma_R(\theta,\theta')=\gamma_R(\theta',\theta)$. For the case of no applied or intrinsic field, as discussed in this paper, $\gamma_j(\theta,\theta')$ is real.

In fact, as analyzed in detail in Ref. [16], the non-phase-matched terms vary rapidly with z (of the order of the optical wavelength), contributing very little to the integration over z. They are small and can be neglected for propagation paths greater than a few hundred micrometers. Thus in our analysis the neglecting of the non-phase-matched terms in Eqs. (10) is reasonable.

Equations (10a) and (10b) are the fundamental equations of our theory. This set of first-order differential equations, together with the appropriate boundary conditions, makes up our mathematical model for the self-pumped phase conjugation in photorefractive crystals. The boundary conditions are considered as follows. In experiments, only the forward beam F is externally input into the crystal at entrance face $z=0$. Due to the unevenness of the crystal surfaces and inhomogeneities and/or defects within the crystal, the scattered light is generated in every direction (both forward and backward) at both entrance face $z=0$ and exit face $z=L$, and within the crystal. In addition, the reflection of the forward beam F at exit face $z=L$ also generates the noise for backward beam B. In real experiments, this reflection at exit face $z=L$ makes a major contribution to the seed for backward beam. Therefore we assume that at face $z=0$, in addition to the plane-wave components of the external input forward beam, we add a noise of $\varepsilon_{10}R(\theta)\sqrt{I_0(0)}$ to every component $f_F(\theta,0)$, where ε_{10} is the forward-scattering coefficient and $R(\theta)$ is a complex function with random magnitude and phase: $|R(\theta)|\leq 1$; at face $z=L$, we introduce a noice of $\varepsilon_{2L}R(\theta)|f_F(\theta,L)|$ to the component $f_B(\theta,L)$, where ε_{2L} is the backward-scattering coefficient. As theoretically shown in Ref. [16], only the scattering at, or near, the surface of the crystal is relevant for seeding the fanning and the backward beam, so we assume that the volume scattering may be neglected. When we consider only two plane-wave components $f_F(\theta,z)$ and $f_F(\theta',z)$ of the forward beam F and two components $f_B(\theta,z)$ and $f_B(\theta',z)$ of the backward beam B, and substitute symbols $f_F(\theta,z)$, $f_F(\theta',z)$, $f_B(\theta,z)$ and $f_B(\theta',z)$ with A_4, A_1, A_3, and A_2 in Eqs. (10), we recover the well-known coupled-wave equations of the four-wave mixing [2].

III. NUMERICAL RESULTS

Our task is to solve equations presented above with split boundary conditions on two opposite crystal faces. We shall do this numerically, using the method we recently applied to study the spatial fidelity of externally pumped phase conjugation [17]. The spatial frequency distribution $f_F(\theta,0)$ is obtained by the fast-Fourier transform. The coupled-wave equations (10a) and (10b) are solved by the Runge-Kutta method. And the total electric-field amplitude $A(x,z)$, Eq. (3), within the crystal is simulated using inverse fast-Fourier transform. In the calculation of $f_F(\theta,0)$, we use 2^{16} Fourier components. In order to save computation resources and time, we use only 1024 components to integrate Eqs. (10), i.e., we take one in every 64 components. To obtain the total amplitude $A(x,z)$, we again use 2^{16} components by interpolating the values between the calculated components. Some results have been checked by use of 2048 components in integration of Eqs. (10). The parameters of the nominal undoped $BaTiO_3$ and the cerium-doped $BaTiO_3$ are taken as in Table I [18,19].

In order to evaluate the merit of the SPPC, we define the phase-conjugate reflectivity as

$$R=\frac{\sum_\theta |f_B(\theta,0)|^2}{\sum_\theta |f_F(\theta,0)|^2} \tag{12}$$

TABLE I. Parameters of nominal undoped $BaTiO_3$ and cerium-doped $BaTiO_3$.

Parameters	Undoped $BaTiO_3$	$BaTiO_3$:Ce
Refractive indices	$n_o=2.488$	$n_o=2.404$
	$n_e=2.424$	$n_e=2.316$
Charge q	1.6×10^{-19} C	1.6×10^{-19} C
Electro-optic	$r_{13}=33$ pm/V	$r_{13}=9.35$ pm/V
coefficients	$r_{33}=124$ pm/V	$r_{33}=85$ pm/V
	$r_{42}=1640$ pm/V	$r_{42}=1770$ pm/V
Dielectric constants	$\varepsilon_a=3600$	$\varepsilon_a=4600$
	$\varepsilon_c=135$	$\varepsilon_c=130$
Number density of mobile charge carriers N	2×10^{22} m^{-3}	8×10^{22} m^{-3}

and the spatial fidelity as [17,20]

$$\mathcal{F}=\frac{\sum_{\theta} f_F(\theta,0)f_B(\theta,0)+\text{c.c.}}{2\left[\sum_{\theta}|f_F(\theta,0)|^2\sum_{\theta}|f_B(\theta,0)|^2\right]^{1/2}}, \tag{13}$$

where the range of summations over θ is determined by the spatial frequency content of the input forward beam F at entrance face $z=0$. Note that if the output beam B at face $z=0$ is exactly conjugate to the input beam F, i.e., $f_B(\theta,0)=R'f_F^*(\theta,0)$, where R' is a factor that is independent of the angle θ, then $\mathcal{F}=1$. In terms of spatial amplitude, Eqs. (12) and (13) can be rewritten as

$$R=\frac{\int|A_B(x,0)|^2dx}{\int|A_F(x,0)|^2dx}, \tag{14}$$

and

$$\mathcal{F}=\frac{\int A_B(x,0)A_F(x,0)dx+\text{c.c.}}{2\left[\int|A_F(x,0)|^2dx\int|A_B(x,0)|^2dx\right]^{1/2}}, \tag{15}$$

where integrations are taken over the transverse dimension x.

A. Properties of the fanning effect

In this subsection, we consider the fanning effect. This means that we consider only the propagation of the forward beam F omitting the backward beam B (or taking $\varepsilon_{2L}=0$). Figure 2 shows the spatial intensity distribution inside an undoped $BaTiO_3$ crystal and its output intensity profile at far field for input Gaussian beam $A_F(x,0)=A_{F0}\exp(-x^2/w_0^2)$, with the beam waist $w_0=0.2$ mm. It is seen that the fanning effect is strong, and that the beam follows a curved path. When the input beam waist w_0 is reduced, the fanning effect is also reduced. This can be seen by comparison of Figs. 2 and 3, where we show the intensity distribution in

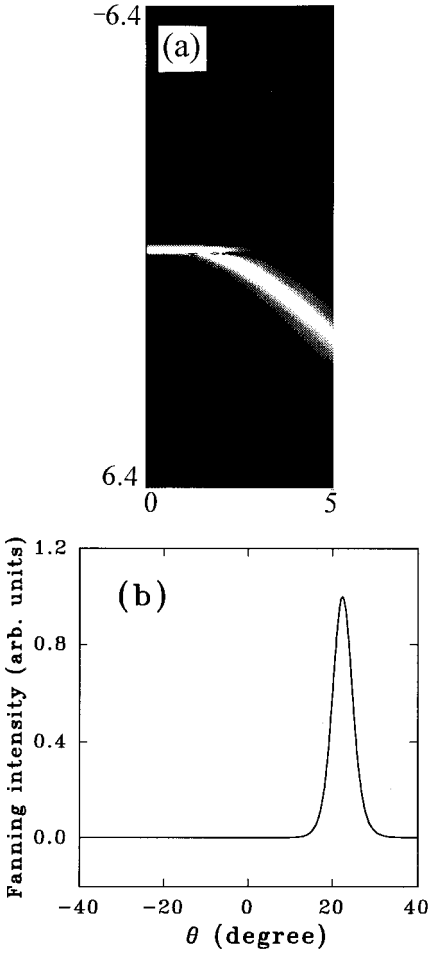

FIG. 2. (a) Numerical simulation of the beam path inside a nominal undoped $BaTiO_3$ crystal. (b) Output intensity profile at far field. Beam waist $w_0=0.2$ nm, $\alpha=0°$, $\beta=35°$, $\varepsilon_{10}^2=1\times10^{-6}$, $L=5$ mm, and $\alpha_L=0$. Without loss of generality, we take the magnitude $|R(\theta)|=1$ both here and later.

the undoped $BaTiO_3$ crystal for a very small waist $w_0=0.002$ mm. From Fig. 3 we also note that as the beam propagates in the crystal it shifts to the c axis and diffracts quickly, with the fanning gradually occurring. All these results are in good agreement with previous experimental observations.

We now examine the influence of the seed level ε_{10} on the fanning effect. The numerical results show that the in-

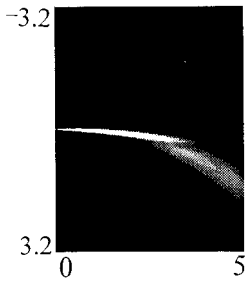

FIG. 3. Numerical simulation of the beam path inside a nominal undoped $BaTiO_3$ crystal for input beam waist $w_0=0.002$ mm, $\alpha=0°$, $\beta=35°$, $\varepsilon_{10}^2=1\times10^{-6}$, $L=5$ mm, and $\alpha_L=0$.

FIG. 4. Numerical simulation of the beam path inside a $BaTiO_3$: Ce crystal for self-pumped phase conjugation. $w_0=0.2$ mm, $\alpha=5.4°$, $\beta=35°$, $\varepsilon_{10}^2=1\times10^{-6}$, $\varepsilon_{2L}^2=3\times10^{-6}$, $L=5$ mm, and $\alpha_L=0$.

crease of the seed level ε_{10} enhances the fanning effect. In other words, the beam begins to bend toward the c axis at smaller longitudinal distance z for larger seed level ε_{10} than for smaller ε_{10}, and the output fanning intensity distribution versus the angle is nearer to the c axis for larger ε_{10} than for smaller ε_{10}. However, the influence of the seed level on the beam fanning is not very strong. As an example, for input Gaussian beam waist $w_0=0.3$ mm ($\alpha=0°$ and $\beta=18°$), the beam inside an undoped $BaTiO_3$ crystal begins to bend at $z\sim2$ mm for seed level $\varepsilon_{10}^2=10^{-5}$ and $z\sim2.6$ mm for $\varepsilon_{10}^2=10^{-6}$, and the angles at which the output fanning intensity ($L=5$ mm) maximizes are $\theta\sim11.5°$ and $\theta\sim8.7°$, respectively. When there exists no seed. (i.e., $\varepsilon_{10}=0$) the fanning effect can be negligible.

B. Properties of the self-pumped phase conjugation

Having discussed the fanning effect, we then consider the self-pumped phase conjugation. For this purpose, we add a noise at $z=L$. In Fig. 4 we demonstrate the total intensity distribution within the crystal for the input Gaussian beam, with the beam waist $w_0=0.2$ mm. The output phase-conjugate reflectivity is 70.1%. The picture in Fig. 4 shows good agreement with the beam path observed by the experiment (see the photograph in Fig. 14). In order to see the merit of the phase conjugation, we use the input image-bearing beam with a rectangular distribution amplitude, i.e.,

$$A_F(x,0)=\begin{cases}\text{const} & -d/2\leqslant x\leqslant d/2\\ 0, & |x|>d/2,\end{cases}\tag{16}$$

instead of a Gaussian distribution. This is because the rectangular distribution has a wider range of spatial frequency content than a Gaussian distribution. In addition, we introduce a phase change in the spatial frequency space of the input beam, as an example, adding a Gaussian distribution phase to every frequency component $f_F(\theta,0)$: $f_F(\theta,0)\times A\cos(-i\theta^2/\theta_0^2)$, where A and θ_0 are constants. Figures

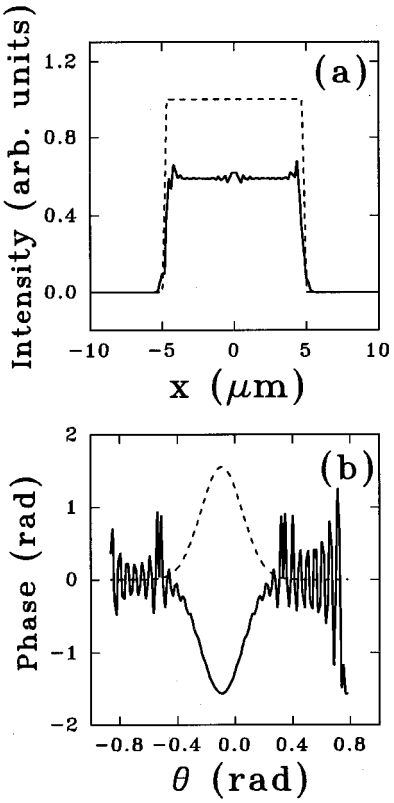

FIG. 5. (a) Output phase-conjugate intensity distribution (solid curve) and input intensity distribution (dashed curve) in real space. (b) Output phase of the phase-conjugate beam (solid curve) and input phase of the image-bearing beam (dashed curve) in spatial frequency space $d=10\,\mu$m, $\alpha=54°$, $\beta=35°$, $\varepsilon_{10}^2=1\times10^{-6}$, $\varepsilon_{2L}^2=3\times10^{-6}$, $L=5$ mm, and $\alpha_L=0$.

5(a) and 5(b) show, respectively, the output intensity and output phase of the phase-conjugate beam, with the given input ones shown by the dashed curves. The reflectivity is 59.2%, and the spatial fidelity is 0.998. It is noted that the output phase is nearly exactly conjugate to the input phase. Another point to note is that the reflectivity of the phase conjugation for an input image-bearing beam which has a wider range of spatial frequency content is smaller than for an input Gaussian beam, which has a narrower range of spatial frequency content. This is consistent with experimental results (see Sec. IV).

From the above results we infer that both the transmission gratings, which are formed between different plane-wave components of the forward beam (and/or those of the backward beam), and the reflection gratings, which are formed between plane-wave components of the forward beam and those of the backward beam, are necessary to generate the phase conjugation. In more detail, it can be described as follows. When an extraordinary beam is input into a photorefractive crystal, its different Fourier plane waves, superimposed by random noise, form a multitude of transmission gratings. This results in the energy transferring (or diffracting) from a wave which has a wave vector at larger angle with respect to the c axis to the wave at smaller angle. Correspondingly, in real space, the beam path bends toward the c axis (see Fig. 2). With the inclusion of the backward noise, reflection gratings are formed between the forward plane

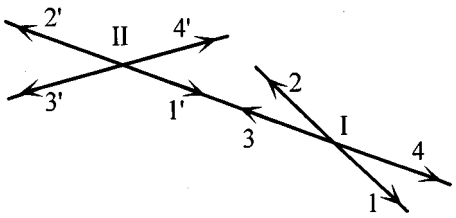

FIG. 6. Schematic diagram to illustrate the generation of the phase conjugation described in the text.

waves and the backward plane waves. The backward waves are then amplified at the expense of the forward waves. In addition, the intensity diffracts from the backward plane wave, which has a wave vector at larger angle with respect to the c axis than that at smaller angle by the above-mentioned transmission gratings, which are now intensified by the backward plane waves. In real space, the backward beam retraces the beam path of the forward beam. Thus the generation of the phase-conjugate beam may be phenomenologically described through the following process. At any longitudinal position z, there exists a multi-four-wave-mixing configuration which can be regarded as an extension of the four-wave mixing. As the backward plane waves propagate, this multi-four-wave mixing occurs continuously. Figure 6 gives a sketch to illustrate this process. At position I, the phase conjugate wave 3 or wave 4 is produced with waves 1 and 2 as pump waves, whereas at position II wave 3 (i.e., wave $2'$) then serves as a pump wave for phase conjugate wave $3'$. Through this continuous process the phase-conjugate beam of the input beam is finally generated at the entrance surface $z=0$.

Since in our model the noise (or seed) is an indispensable condition for the generation of the self-pumped phase conjugation, it is necessary to discuss their dependence on the seed level. Now both the seed ε_{10} and ε_{2L} are relevant. In order to see the influence of each seed on the SPPC reflectivity and spatial fidelity, we keep ε_{10} constant while changing ε_{2L}, and keep ε_{2L} constant while changing ε_{10}. The results are shown in Fig. 7, where we take the input field amplitude as a rectangular distribution, Eq. (16), with width $d=10$ μm. (In all the later discussions we will take the input field amplitude as this distribution.) As anticipated, the SPPC reflectivity increases greatly with the increase of the seed level ε_{2L}. The seed ε_{10} also has an influence on the reflectivity, and the reflectivity decreases with an increase of the seed level ε_{10}. But its effect is much smaller than the seed ε_{2L}. For example, an increase of the seed level ε_{2L}^2 from 1×10^{-6} to 1×10^{-5} leads to an increase of the reflectivity from 0.201 to 0.635, whereas an increase of ε_{2L}^2 from 1×10^{-6} to 1×10^{-5} leads to a decrease of the reflectivity from 0.54 to 0.44. From Fig. 7(b) we note that the SPPC spatial fidelity is insensitive to both the seed levels ε_{10} and ε_{2L}. Speaking more exactly, the spatial fidelity increases with the increase of the seed ε_{2L} and the decrease of the seed ε_{10}, or the fidelity increases with the decrease of the reflectivity. From the above discussions we can thus conclude that, of the two seeds ε_{10} and ε_{2L}, the seed ε_{2L} is the more sensitive factor to influence the self-pumped phase conjugation, and that it is more sensitive to the SPPC reflectivity.

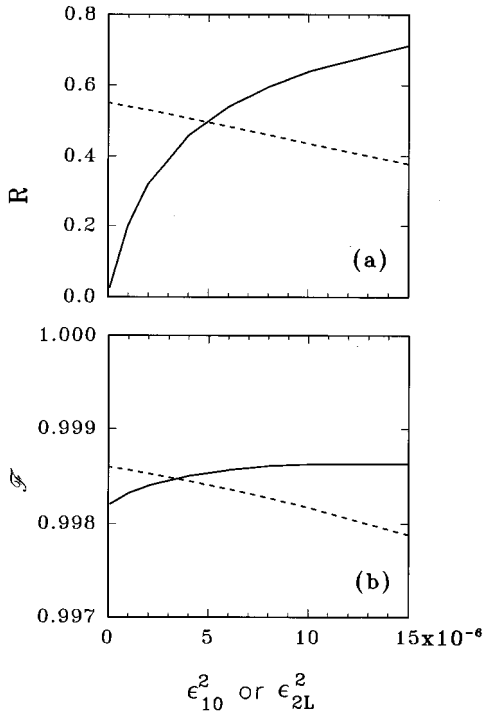

FIG. 7. (a) SPPC reflectivity and (b) spatial fidelity vs the seed level ε_{10}^2 for fixed $\varepsilon_{2L}^2=6\times10^{-6}$ (dashed curves) and the seed level ε_{2L}^2 for fixed $\varepsilon_{10}^2=1\times10^{-6}$ (solid curves). $\alpha=0°$, $\beta=35°$, $L=4.6$ mm, and $\alpha_L=0$.

C. SPPC reflectivity and spatial fidelity versus externally controlled parameters

In this subsection we will present our numerical results of the SPPC reflectivity and spatial fidelity as a function of the incident angle, and their dependence on the position of the incident beam upon the crystal entrance face (or the position of incidence), following the experimental results of Ref. [7]. We will also present the results of the reflectivity and fidelity as a function of the input wavelength, in order to explain the experimental results that the SPPC reflectivity is higher at a wavelength of $\lambda=632.8$ nm than at $\lambda=514.5$ nm (see Sec. IV).

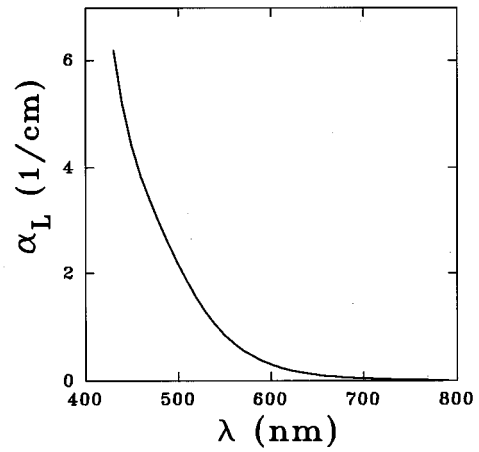

FIG. 8. Absorption spectra of $BaTiO_3$ for a cerium-doping concentration of 15 ppm.

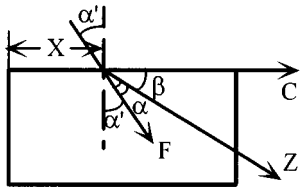

FIG. 9. Definition of the position of incidence X and the incident angle α' in a 0°-cut $BaTiO_3$:Ce crystal.

To make a quantitative comparison with experimental results, we should take into consideration the linear absorption of the crystal. The experimental measurement of the absorption coefficient of a 15-ppm cerium-doped $BaTiO_3$ at very low intensity is given in Fig. 8. It is known that the absorption coefficient is increased at high intensity [21,22]. Therefore in our simulation of the experimental results of Ref. [7], we take an absorption coefficient larger than that given in Fig. 8, as an example, we take $\alpha_L = 0.4\ \mathrm{mm}^{-1}$ at a wavelength of $\lambda = 514.5$ nm.

First, we consider the dependence of SPPC reflectivity and spatial fidelity on the position of incidence. Similar to the experiments in Ref. [7], we use a 0°-cut $BaTiO_3$:Ce crystal, with its two dimensions in the paper plane as $8 \times 6.85\ \mathrm{mm}^2$, and the c axis along the 8-nm dimension. The distance X is defined as in Fig. 9. The coordinate $+z$ axis is taken in the direction which makes an angle of 30 ° with the c axis. We take the angle $\alpha = 15°$ inside the crystal. The results of the reflectivity and spatial fidelity as a function of X are shown in Fig. 10. We see that the reflectivity has a dependence on X similar to that of the experimental results, as shown in Fig. 3 of Ref. [7]. The reflectivities are high at middle range of X, whereas at small and large X the reflectivities are low. This can be understood as follows. The larger X is, the smaller the interaction length L, and therefore the smaller the phase-conjugate reflectivity, whereas at smaller X the propagation distance L is long, and therefore

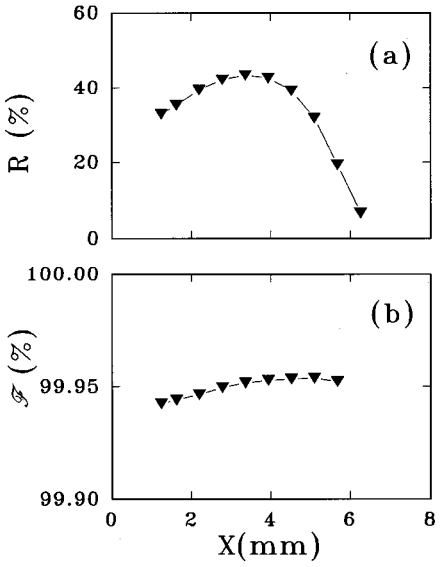

FIG. 10. Dependence of the (a) SPPC reflectivity and (b) the spatial fidelity on the X. $\varepsilon_{10}^2 = 1 \times 10^{-6}$, $\varepsilon_{2L}^2 = 1 \times 10^{-4}$, and $\alpha_L = 0.4\ \mathrm{mm}^{-1}$.

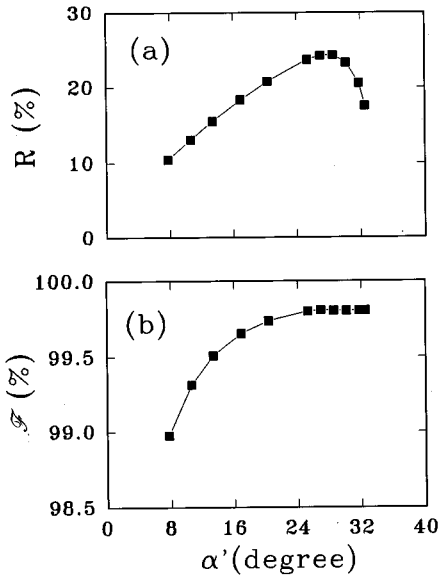

FIG. 11. (a) SPPC reflectivity and (b) spatial fidelity as a function of incident angle α'. $\varepsilon_{10}^2 = 1 \times 10^{-6}$, $\varepsilon_{2L}^2 = 4 \times 10^{-6}$, and $\alpha_L = 04\ \mathrm{mm}^{-1}$.

the linear absorption is large, which results in the backward seed $\varepsilon_{2L} |f_F(\theta, L)|$ being reduced. Thus the SPPC reflectivity decreases due to the large absorption and the small backward seed level. The spatial fidelity is very high (larger than 0.999), and it changes very little with a change of the distance X. In general, it increases with an increase of X (or decrease of the interaction length L).

We next consider the SPPC reflectivity and spatial fidelity as a function of the incident angle α', which is defined as in Fig. 9 (similar to the definition in Ref. [7], where it is the incident angle outside the crystal). The coordinate $+z$ axis is assumed to be in a direction which makes an angle of $\beta = 45°$. The length $L = 4$ mm. Our numerical results are shown in Fig. 11. From Fig 11(a) we see that the curve shows good agreement with the experimental one, as shown in Fig. 2 of Ref. [7]. The reflectivity increases with the increase of angle α', and maximizes at $\alpha' \sim 28°$. Then it declines with a further increase of the angle α'. From Fig. 11(b) we see that the spatial fidelity increases with an increase of the incident angle α' (or a decrease of the angle between the c axis and the propagation direction of the incident beam). Furthermore, the smaller the angle α' becomes, the faster the spatial fidelity decreases.

Finally we consider the SPPC reflectivity and spatial fidelity as functions of the input wavelength λ. The dependence of the refractive indices n_o and n_e on λ are obtained by the Sellmeier equation

$$n_{e,o}^2 = n_0 + \frac{A}{\lambda^2 - B} + C\lambda^2, \tag{17}$$

TABLE II. Sellmeier parameters at room temperature.

$n_{e,o}$	n_0	A	B	C
n_e	5.188 16	$1.366\,92 \times 10^7$	$7.035\,93 \times 10^6$	$-4.624\,42 \times 10^{-10}$
n_o	5.397 85	$1.525\,65 \times 10^7$	$8.180\,33 \times 10^6$	-9.8523×10^{-10}

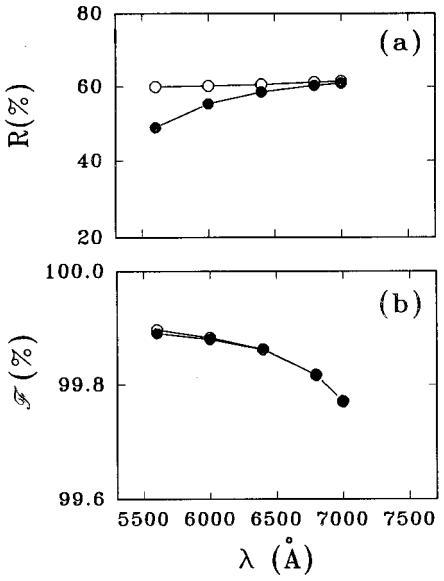

FIG. 12. (a) SPPC reflectivity and (b) spatial fidelity vs the input wavelength λ. The lines with hollow dots are for $\alpha_L=0$ and the lines with filled dots are for α_L given in Fig. 8. $\alpha=0°$, $\beta=35°$, $\varepsilon_{10}^2=1\times10^{-6}$, $\varepsilon_{2L}^2=1.6\times10^{-5}$, and $L=4$ mm.

where values of n_0, A, B, and C are given in Table II. λ is in units of Å. Since the spectral dependence of the electro-optic coefficient r_{mn}, the dielectric constants ε_a and ε_c, and the number density of mobile charge carriers N have not yet, been measured, we assume that they have a negligible dependence on λ in our calculation. Because our purpose is to explain the dependence of the SPPC reflectivity and spatial fidelity on the wavelength qualitatively, we simply adopt the absorption coefficient α_L at different wavelengths, as given in Fig. 8. The results for the reflectivity and fidelity versus the wavelength λ are shown in Fig. 12, where the curve with hollow dots is for the case of negligible linear absorption, i.e., $\alpha_L=0$, and the curve with filled dots is for the case of the linear absorption coefficients taken from Fig. 8. We see that the reflectivity decreases with the decrease of the wavelength λ. Due to the larger linear absorption at shorter wavelength, the reflectivity decreases faster with a decrease of the λ. This is consistent with our experimental results that the reflectivity is larger at a wavelength of $\lambda=632.8$ nm ($R=32.5\%$) than at $\lambda=514.5$ nm ($R=25.6\%$). Contrary to the reflectivity, the spatial fidelity decreases with an increase of the wavelength. Furthermore, the longer the wavelength becomes, the faster the fidelity decreases.

IV. EXPERIMENTS

In order to check our numerical results, in this section we present some experimental results performed on a $BaTiO_3$ crystal of cerium-doping concentration 50 ppm, which was grown at the Institute of Physics, Chinese Academy of Sciences. The dimensions of the crystal are $5.92\times3.30\times3.15$ mm^3, with the c axis along its longest dimension.

We use two wavelengths of 514.5 and 632.8 nm in the experiments. The experimental arrangement is shown in Fig. 13. An extraordinary beam from a He-Ne laser or an A_r^+ laser passes through a variable neutral-density (ND) filter, a lens ($L1$), and a beam splitter (BS), and is then incident upon the $BaTiO_3$:Ce crystal at an angle of 75° with respect to the normal to the crystal surface. The power of the phase conjugate beam, after reflection from the beam splitter BS, is measured by a detector (D).

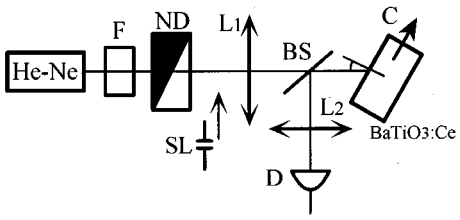

FIG. 13. Experimental setup. F, Faraday isolator; ND, variable neutral-density filter; $L1$ and $L2$, lens; BS, beam splitter; D, detector; SL, slit.

For the wavelength of 632.8 nm, the power of the incident beam is ~0.65 mW, and the beam width is ~0.5 mm (Gaussian beam) as it enters the crystal. After about 45 min of the beam incident upon the crystal, a stable SPPC reflectivity of ~32.5% is obtained. Figure 14 is the photograph of the beam path inside the crystal at the steady state, which shows clearly that it is a curved one. This is in good agreement with our numerical simulation (see Fig. 4). It is also seen that there is no total internal reflection at a corner of the crystal as is in the case of the ''cat'' mirror, which support our model.

For a wavelength of 514.5 nm, the power of the incident beam is ~2 mW, and the Gaussian beam width ~0.5 nm as it enters the crystal. After about 20 min of the beam incident upon the crystal, the phase-conjugate beam attains its steady state, with a reflectivity of ~25.6%. The steady beam path is similar to the photograph of Fig. 14. The smaller reflectivity at $\lambda=514.5$ nm than that at $\lambda=632.8$ nm is consistent with the numerical results (see Sec. II B).

Instead of the Gaussian beam with an image-bearing beam, we insert a slit (SL) into the beam path (see Fig. 13). The slit with width $d=120$ μm can be effectively regarded as infinitely long in the direction perpendicular to the plane of incidence. The lens ($L1$) images the slit on the crystal, and collects up to a thirtieth-order spatial frequency component of the slit. The intensity of the beam as it enters the

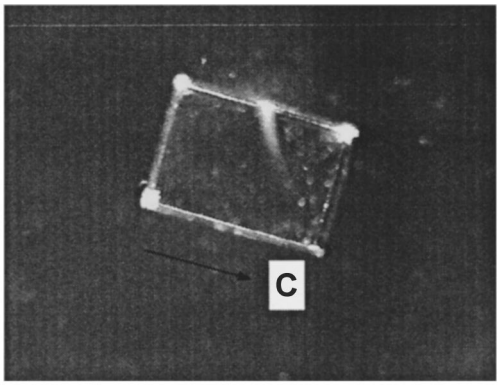

FIG. 14. Photograph of the beam path inside the $BaTiO_3$:Ce crystal after the buildup of the steady state at a wavelength of 632.8 mm.

crystal are identical with those of Gaussian beam ($\sim$0.65 mW). After about 45 min we obtain a stable SPPC reflectivity of $\sim$22.3%. It is smaller than the one obtained with the Gaussian beam. This is in agreement with our numerical results (see Sec. III B).

V. CONCLUSIONS

In summary, we presented a model for the beam fanning and the self-pumped phase conjugation in photorefractive crystals. The numerical simulation of the curved beam path inside $BaTiO_3$:Ce crystals and the high-fidelity self-pumped phase-conjugate beam show good agreement with the experiments. The seed effect on the beam fanning and the self-pumped phase conjugation were discussed, which shows that the SPPC reflectivity is sensitive only to the backward seed at the exit face of the crystal, whereas the spatial fidelity is insensitive to the seeds at both the input and the exit faces. The SPPC reflectivity and the spatial fidelity versus the incident angle, the position of the incident beam upon the crystal input face, and the wavelength of the input beam were numerically studied, which show good agreement with the previous and our experimental results.

ACKNOWLEDGMENTS

This research was supported by the National Natural Science Foundation of China and by the Nonlinear Project of China.

[1] See, for example, Y. Fainman, E. Klancik, and S. H. Lee, Opt. Eng. **25**, 228 (1986); P. Yeh, IEEE J. Quantum Electron. **QE-25**, 484 (1989).
[2] See, for example, M. Cronin-Golomb, B. Fischer, J. O. White, and A. Yariv, IEEE J. Quantum Electron **QE-20**, 12 (1984); *Photorefractive Materials and Their Applications II*, edited by P. Gunter and J. P. Huignard (Springer-Verlag, Berlin, 1989), Chaps. 4–6.
[3] J. Feinberg, Opt. Lett. **7**, 486 (1982).
[4] A. V. Nowak, T. R. Moore, and R. A. Fisher, J. Opt. Soc. Am. B **5**, 1864 (1988).
[5] T. Y. Chang and R. W. Hellwarth, Opt. Lett. **10**, 408 (1985).
[6] R. A. Mullen, D. J. Vickers, L. West, and D. M. Pepper, J. Opt. Soc. Am. B **9**, 1726 (1992).
[7] Y. Zhu, C. Yang, M. Hui, X. Niu, J. Zhang, T. Zhou, and X. Wu, Appl. Phys. Lett. **64**, 2341 (1994).
[8] K. R. MacDonald and J. Feinberg, J. Opt. Soc. Am. **73**, 548 (1983).
[9] A. A. Zozulya, M. Saffman, and D. Z. Anderson, Phys. Rev. Lett. **73**, 818 (1994); A. A. Zozulya, G. Montemezzani, and D. Z. Anderson, Phys. Rev. A **52**, 4167 (1995).
[10] J. F. Lam, Appl. Phys. Lett. **46**, 909 (1985).
[11] P. Xie, J. H. Dai, P. Y. Wang, and H. J. Zhang, Appl. Phys. Lett. **69**, 4005 (1996).
[12] J. Feinberg, J. Opt. Soc. Am. **72**, 46 (1982).
[13] M. Segev, B. Crosignani, A. Yariv, and B. Fischer, Phys. Rev. Lett. **17**, 923 (1992).
[14] C. Xu, D. Statman, and J. K. McIver, J. Opt. Soc. Am. B **9**, 1825 (1992).
[15] N. V. Kukhtarev, V. B. Markov, S. G. Odulov, M. S. Soskin, and V. L. Vinetski, Ferroelectrics **22**, 949 (1979).
[16] M. Segev, D. Engin, A. Yariv, and G. C. Valley, Opt. Lett. **18**, 956 (1993); D. Engin, M. Segev, S. Orlov, A. Yariv, and G. C. Valley, J. Opt. Soc. Am. **B 11**, 1708 (1994).
[17] P. Xie, J. H. Dai, P. Y. Wang, and H. J. Zhang, J. Opt. Soc. Am. B (to be published).
[18] Y. Zhu, P. Bernasconi, M. Zgonik, and P. Gunter, J. Synth. Cryst. **23**, 242 (1994) (in Chinese).
[19] P. Yeh, *Introduction to Photorefractive Nonlinear Optics* (Wiley, New York, 1993).
[20] G. C. Valley, J. Opt. Soc. Am. B **9**, 1440 (1992).
[21] C. Yang, Y. Zhang, P. Yeh, Y. Zhu, and X. Wu, Opt. Commun. **113**, 416 (1995).
[22] S. Orlov, M. Segev, A Yariv, and R. R. Neurgaonkar, Opt. Lett. **19**, 1293 (1994).